




Flows in horizontal thermohaline convection with differential diffusion

J. A. Whitehead


To cite this article: J. A. Whitehead (2021): Flows in horizontal thermohaline convection with differential diffusion, Geophysical & Astrophysical Fluid Dynamics, DOI: [10.1080/03091929.2021.1888375](https://doi.org/10.1080/03091929.2021.1888375)


To link to this article: <https://doi.org/10.1080/03091929.2021.1888375>

 View supplementary material [↗](#)

 Published online: 02 Mar 2021.

 Submit your article to this journal [↗](#)

 Article views: 30

 View related articles [↗](#)

 View Crossmark data [↗](#)



Flows in horizontal thermohaline convection with differential diffusion

J. A. Whitehead

Physical Oceanography Department, Woods Hole Oceanographic Institution, Woods Hole, MA, USA

ABSTRACT

Oceanographers use the term “differential diffusion” to express a greater value of bulk turbulent diffusivity of temperature within the ocean than the value of bulk diffusivity of salinity, the ratio quantified by Lewis number. Investigation of horizontal thermohaline convection at Prandtl number 1 and infinity over the range $1 < Le \leq 10$ reveals a variety of new flow patterns. The chamber has a linearly changing temperature T and salinity S along the top extending from the cold, fresh “polar” end to the hot, salty “tropics” end. It has an aspect ratio of 8 and sides and bottom are insulated and impermeable. Five transition flow patterns occur with little hysteresis for a fixed salinity Rayleigh number Ras of order 10^5 as Rayleigh number Ra changes from 3.2×10^6 down to 1. They are: 1. A steady T-cell with sinking at the cold end flowing into a bottom flow that feeds up into a top thermal boundary layer. 2. Salty blobs in the boundary layer that amplify and move from the hot to cold end. Each cold end arrival triggers a sudden increase in overturning velocity. 3. A “stripes” pattern where top to bottom cells (alternating T and S cells) move toward the cold end. 4. An S-cell that is a mirror image of the T-cell near the top along with small T-cells lying at the bottom that move toward the cold end. 5. A steady S-cell. Each pattern has a distinct volumetric signature in a $T-S$ diagram. Ranges of Ra with various patterns are sizeable at $Ras = 7.5 \times 10^5$ if $Le > 4/3$ but insensitive to Pr . Balanced convection at $Ra = Ras > 10^6$ adopts a large unsteady supercell containing smaller T and S cells. Exact ranges of the supercell are unknown. Since differential diffusion produces a large collection of flows compared to thermal convection alone, it might produce unexpected new results if added into numerical models of the ocean.

ARTICLE HISTORY


Received 3 April 2020
Accepted 7 February 2021


KEYWORDS

Differential diffusion;
horizontal convection;
double diffusion; deep ocean
convection; unsteady flows

1 Introduction

Horizontal convection is the term used by Stern (1975) for the simplest known model for the vertical circulation of the ocean. It follows the laboratory experiment of Rossby (1965) and consists of a nonrotating rectangular chamber with water subjected to a surface temperature distribution to mimic the equator to pole temperature difference of the

CONTACT J. A. Whitehead  jwhitehead@whoi.edu

 Supplemental data for this article can be accessed here. <https://doi.org/10.1080/03091929.2021.1888375>

© 2021 Informa UK Limited, trading as Taylor & Francis Group

atmosphere. The dynamics includes viscous stress, inertia, and thermal convection with the Boussinesq approximation. Flow in this model produces a good first-order approximation of the temperature structure of the ocean with sinking in a narrow region at the coldest end. The deep fluid spreads along the bottom toward the warm end and rises to the surface in a thermal boundary layer (an analog of the ocean thermocline). Horizontal convection captures the thermal and vertical circulation structure of the ocean, but the velocity scales incorrectly because it lacks many realistic oceanic effects such as rotational dynamics, wind-driving, turbulent eddy effects, multiple basins, the Southern Ocean, non-linear equation of state for seawater and so forth. Modern ocean models that include some of these effects whether they be numerical (e.g. Marshall and Speer 2012) or conceptual (Gnanadesikan 1999) capture both the lateral ocean circulation and the speeds much better.

Because of its simplicity, horizontal convection continues to attract attention. It has a long pedigree (Beardsley and Festa 1972, Paparella and Young 2002, (concerning the provocative Sandstrom's theorem), Winters and Young 2009, Hughes *et al.* 2013, Whitehead 2017 and references therein). It is governed by two dimensionless numbers, the Rayleigh number Ra and the Prandtl number Pr . At increasingly large Ra , the power laws, structure, speed and effects of turbulence in horizontal convection for a variety of values of Pr have been of considerable interest.

This study extends parameters for horizontal convection in another direction by considering water with dissolved salt where there are distributions of both temperature and salinity imposed along the top surface boundary. This introduces two additional governing parameters, the salt Rayleigh number Ras and the Lewis number $Le = \kappa/\kappa_S$, where κ is thermal diffusivity and κ_S is salinity diffusivity. This definition of Le is common in oceanography but some engineering definitions differ.

Our objective is to investigate horizontal convection over sizeable ranges of Ra , Ras , and Le . It is well-known that T and S variations in the ocean are globally important (Sverdrup *et al.* 1942), yet most studies of both horizontal convection and ocean circulation utilise only a single value of internal diffusivity for temperature and salinity. New features in horizontal convection occur with differing types of boundary conditions for T and S (Whitehead 2017) and here we ask “does horizontal convection driven by T and S with the same boundary conditions but with different values of their diffusion possess new flows, and if so, what are they?”

Both the terms differential diffusion and, more commonly, double diffusion are used to describe cases with $Le \neq 1$. Here, the term *differential diffusion* is used because the two diffusivities are in the context of oceanic horizontal convection. They represent two Austausch coefficients from internal turbulent mixing within the ocean. The fluid mechanics of both is the same as molecular double diffusion (Turner 1973, Schmitt 1994) so our numerical advection–diffusion equations are identical to the molecular diffusion equations. The emphasis here is on the influence of different “turbulent diffusivities” on flows that are suggestive of large scale ocean circulation. (In addition, the boundary conditions used here differ from numerous ones in the cited double diffusion studies). Another reason we use the term differential diffusion rather than double diffusion is that small-scale double diffusive processes using molecular diffusivity also exist in the ocean (Schmitt 1994). Their contribution to vertical transport in the global budgets is estimated to be small (Merryfield *et al.* 1999). Therefore using “differential” rather than “double” is important.

The concept of differential diffusion within the ocean itself was introduced from both oceanographic data and laboratory measurements by Gargett (1989). The arguments for the existence of $Le > 1$ for bulk diffusivities of salinity and heat in the ocean were strengthened by Gargett (2003), who wrote:

This note reviews existing evidence of differential diffusion as provided by laboratory experiments, numerical simulations, and oceanic observations. Given potentially serious implications for proper interpretation of estimates of diapycnal density diffusivity from both ocean microscale measurements and ocean tracer release experiments, as well as the notable sensitivity of predictive global ocean models to this diffusive parameter, it is essential that this process be better understood in the oceanographic context.

Different rates from turbulent mixing (Gregg *et al.* 2018, Rehmann and Gargett 2018 and references therein) imply a range of values of Le . Laboratory measurements from a variety of experiment configurations clearly show values of turbulent Le ranging from 1 to 3 (Turner 1968, Gargett 2003, Rehmann and Koseff 2004, Whitehead 2016, Gregg *et al.* 2018). A consistent result is that the largest value of Le exists at moderate Reynolds number ($Re \approx 2000$), which is characteristic of many ocean regions. In addition, direct numerical simulations (DNS) of stratified turbulence show clear evidence of $Le > 1$ although runs with high Re using molecular salt diffusivities as in the ocean or laboratory cannot yet be attained. Results to date give turbulent mixing rates that are equivalent to bulk values of turbulent $Le = 3$ (Gargett 2003), and $Le =$ from 1.2 to 2 (Smyth *et al.* 2005).

Differential diffusion directly produces different T and S residence times in the ocean. Therefore, Stommel's classic 1961 box model with abrupt transitions (figure 1(a)) is equivalent to horizontal convection with differential diffusion. Differential diffusion is also a factor in the oscillating instability of stratified fluid by Welander (1989), and probably occurs in laboratory experiments showing abrupt transitions and oscillations (Whitehead *et al.* 2005, Whitehead 2009). It also occurs in binary gases with sideways driving (Nishimura and Morega 2003). In other numerical studies, it is included in ocean box models by Gargett and Ferron (1996) and Gargett (2019), in a large numerical ocean model by Gargett and Holloway (1992), and in another study of localised ocean mixing by Hirst and Cai (1994). All these ocean models are conducted over a narrow range of driving parameters. This motivated this study of differential diffusion in horizontal convection over much wider ranges of parameters. Since many important factors such as earth rotation, multiple basins and the like are missing for this simple study of horizontal convection, results do not apply in detail to ocean modelling. However, the results over wide ranges might show that ignoring differential diffusion and assigning $Le = 1$ in ocean numerical models could be a mistake.

This study uses a simple numerical code for horizontal convection with differential diffusion in a chamber driven by a temperature and salinity distribution along the top. Section 2 explains the geometry and method. Section 3 shows patterns and time dependent flows over sizeable ranges of Ra , Ras and Le . Section 4 contains the particular case where the buoyancies from T and S at the top cancel ($Ra = Ras$ and therefore all variations of T and S and all flows are the results of only differential diffusion. Results extend from marginal values up to $Ra = Ras = 5 \times 10^8$ where a large complicated super cell occurs. Section 5 has discussions of the results in the context of both the ocean itself as well as in the context of other fluid studies.

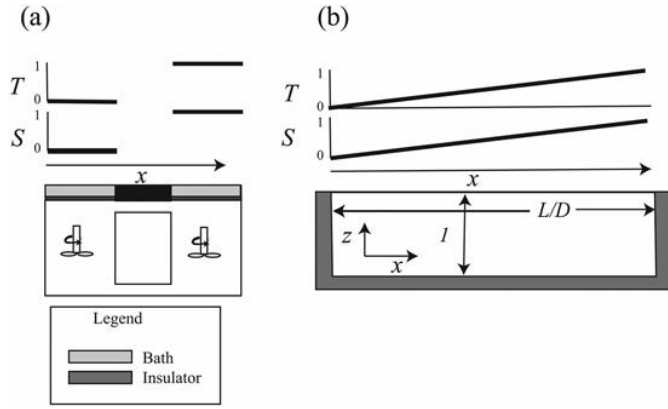


Figure 1 (a) The two-box model that has two connected insulated chambers of mixed water with dimensionless values of T and S diffusing through the lid with different diffusion rates. Stommel (1961) had the diffusion through the sides instead of top. (b) This model. Horizontal convection in a two dimensional insulated rectangular chamber of water with linear changes of T and S along the top and with differential diffusion in the interior.

2 The model and method

Our configuration consists of water in a rectangular chamber of depth D and of length L in the lateral (x) direction along the chamber with z positive upward in the vertical (gravity) direction. A temperature T_0 increases linearly from the top of the left end (like a polar region) to $T_0 + \Delta T$ at the top of the right end (like a tropical region) along with salinity increasing linearly from S_0 to $S_0 + \Delta S$ from left to right. This makes the densest water from T at the left end and the densest water from S at the right end.

The equations governing conservation of mass, momentum, heat, and salt are assigned constant properties except for linear buoyancy terms driven by T and S (Boussinesq approximation). They are transformed to dimensionless form using depth scale D the temperature scale ΔT , the salinity scale ΔS , the velocity scale κ/D , and the time scale D^2/κ (both based on thermal diffusivity κ , see Appendix). The dimensionless chamber (figure 1(b)) has depth 1 and length L/D . Dimensionless temperature and salinity change linearly from 0 to 1 along the top. As discussed in the introduction, the diffusivities in this model are meant to represent bulk properties of the ocean rather than molecular values. However, it might be possible to conduct laboratory experiments of this problem where molecular properties are used.

Using the above scales along with salinity diffusivity κ_S , the dimensionless equations are the same as those with double diffusion

$$\frac{\partial T}{\partial t} + \mathbf{u} \cdot \nabla T = \nabla^2 T \quad (1)$$

$$\frac{\partial S}{\partial t} + \mathbf{u} \cdot \nabla S = Le^{-1} \nabla^2 S \quad (2)$$

Only two-dimensional flows are considered. The vorticity equation is

$$\frac{1}{Pr} \left[\frac{\partial}{\partial t} + \mathbf{u} \cdot \nabla \right] - \nabla^2 \zeta = -Ra \frac{\partial T}{\partial x} + Ras \frac{\partial S}{\partial x} \quad (3)$$

where $\zeta = \partial u / \partial z - \partial w / \partial x$. The equation for a streamfunction is

$$\nabla^2 \psi = \zeta. \quad (4)$$

The five governing dimensionless numbers are: Rayleigh number $Ra = g \Delta T D^3 / \kappa \nu$, salinity Rayleigh number $Ras = g \beta \Delta S D^3 / \kappa \nu$ (note that temperature diffusivity is used), Lewis number $Le = \kappa / \kappa_S$, Prandtl number $Pr = \nu / \kappa$ and chamber aspect ratio L/D . In addition to the two diffusivities that are previously defined, properties of the fluid are as follows: ρ_0 is average density, ν is kinematic viscosity, g is acceleration of gravity, α is the coefficient of thermal expansion, and β is the coefficient of haline contraction.

Boundary conditions are free-slip along all boundaries, linear temperature and salinity profiles in the x direction along the top, and zero fluxes of heat and salinity along the sides and bottom. The free slip condition is admittedly less realistic than zero velocity as imposed by Beardsley and Festa (1972) and Marchal (2007), but it is the simplest condition and therefore can deliver numerous results over very broad ranges of parameters. Finite difference calculations advance in time for numerous runs over a broad range of the parameters. The finite difference numerical scheme is reviewed in the Appendix. Typical evolution of flows as time progresses is not remarkable. An initial adjustment time occurs for each run as T and S diffuses into the chamber and then produces the first flows. Then there is an adjustment time when flows relax to a final state. Evolution of some bulk properties are shown later in this paper (figures 12 and 13). In the case of unsteady flows, enough time is given to measure over many cycles. In some cases, this requires hundreds of time units. The decision of what constitutes final flow was completely empirical, and based on monitoring the many bulk properties such as the evolution of temperature and salinity values midway along the bottom, the extrema of the streamfunction, Nusselt Number Nu for T and the equivalent Nu_S for S , and mean values of T and S .

Concerning resolution, the standard grid size was 32×256 points. Double the number is used for most of the figures and was invoked where precision is needed. With the time step used, the values of speed, details of the T and S distributions, and the transition values between patterns of flow have precisions of a few percent. A comparison for a case with an irregular time-dependent flow using first the present grid size and then twice the number of grid points is in section 3.4 (figure 12). This has perfect reproduction of the pattern of evolution of the maximum value of streamfunction for the first 0.1 time unit (although the values have up to a 10% amplitude difference). After that time, the two flows differ in detail although they have similar patterns of variability. More aspects of the resolution are discussed in the appendix.

3 Results

3.1. Overall coverage

The primary purpose is to investigate the effects of differential diffusion by mapping out the amplitude and pattern of flow over wide ranges of Ra and Ras , up to 5×10^8 and $Le \leq 10$.

Although exploratory experiments started with a variety of aspect ratios, time constraints made it obvious that it was important to pick only one aspect ratio to allow a reasonable number of calculations. The value $L/D = 8$ was selected because it admits the possibility of a number of circulation cells in the lateral direction. It also permits clear views of signals travelling back and forth between the two ends and allows the possibility of any lateral cell migration that might occur. Using larger values is possibly worth doing but not pursued here.

The value of Pr is also restricted. Initially values of both $Pr = 1, 2, 5, 10$ and ∞ were used, but in all cases the patterns of flow proved to be the same for all values and their speeds differed by only a few percent. Ocean applications would generally fall in that range. Therefore, except for some part of figure 2, all calculations are with $Pr = 1$ and no detailed systematic variation of Pr is presented. In all results, the amplitude of maximum streamfunction (an excellent measure of Reynolds number) never exceeded 100 (figure 15). This is too small to evoke issues connected with turbulence in horizontal convection, (Paparella and Young 2002, Scotti and White 2011, Gayen *et al.* 2013, Gayen *et al.* 2014 and citations therein) and therefore Pr dependence and turbulence are topics that are not covered.

This still leaves three dimensionless numbers and full coverage proved to be challenging. For example, even in the limited ranges $10^5 \leq Ras \leq 10^6$, $Ra/Ras < 4$, and $Le \leq 10$, five flow patterns exist. The distribution of these patterns is shown in section 3.2.1. Sections 3.2.2–3.2.6 describe the patterns of flow in detail. Three of those patterns change in time (slowly, on the order of the thermal time scale or longer), which implies that the process producing them is due to differential diffusion of T and S .

Quantitative values of heat transport, salinity transport and speed are presented in section 4 for a large range of Ra up to 5×10^8 . First, simple component flow (Ras set

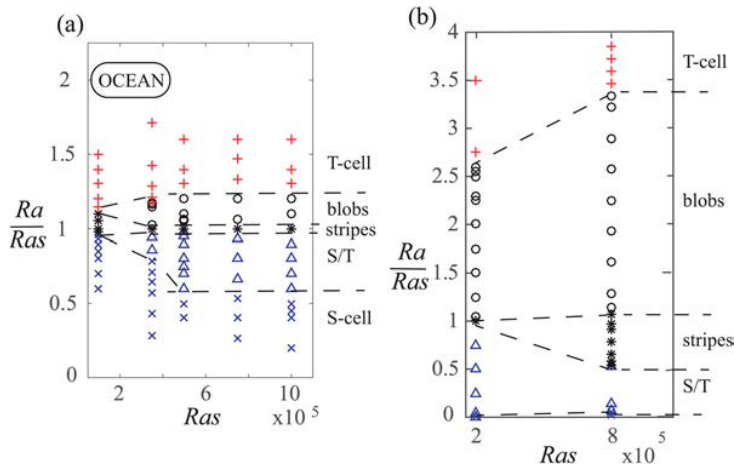


Figure 2 The regions of various patterns of flow in the range $10^5 \leq Ras \leq 10^6$ in a chamber with $L/D = 8$. The flow patterns are: the T-cell (red +), blobs (black o), stripes (black *), S/T (blue Δ), and the S-cell (blue x). Dashed lines separate the different patterns. (a) Results for $Le = 2, Pr = 1$. Best fit parameters for the ocean are indicated in the oblong (see sections 3.2.2 and 4.1). (b) Results for $Le = 10$. These results were calculated for both $Pr = 1$ and $Pr = \infty$ and they were so close to identical that symbols simply replaced each other. (Colour online)

to 10^{-3}) is presented and it has most of the features for $L/D=1$ (Rossby 1998). The asymptote slopes of the values of transport and streamfunction maximum are $\approx Ra^{1/5}$ and therefore similar. Then flows with $Ra = Ras$ over the range from 1 to 10^8 are presented. These flows illustrate most clearly the effects of differential diffusion because buoyancy forcing of T and S cancel each other at the top surface. Virtually all the flows have considerable scatter due to time dependence. At the extreme large and small values of $Ra = Ras$, two new patterns of flow exist.

3.2. Five flow patterns

Five patterns and their ranges are shown in figures 2 and 3. Each pattern is described in more detail in section 3.3. Except near transition, one of the five patterns of flow in figures 2 and 3 is formed within approximately 5 time scales. Three of them are time-dependent and in those cases the calculations are conducted after transition for a time long enough to view many cycles of the time dependent flow. Runs typically take many tens of diffusion times. figure 2(b) includes points for both $Pr=1$ and ∞ but results were identical so two symbols indicating Pr are not included. Other calculations with values of $Pr=2, 5$, and 10 , showed no change in pattern. Therefore, all calculations beyond those in figure 2(b) are with $Pr=1$.

Figure 2 shows that there are very different results for different Le . Therefore, the ranges depend on Le and this prompted a collection of runs at a number of values of Le . Results are shown in figure 3. (They are plotted versus Le^{-1} because this gave more uniform spread on the graph.) Ranges are large at $Le=10$ and become relatively small as Le approaches 1.33. The range for all 5 patterns has shrunk to $Ra/Ras \cong \pm 5$, at $Le=1.1$ and down to $Ra/Ras \cong \pm 1$ at $Le=1.01$ (both are only plotted as single points on figure 3).

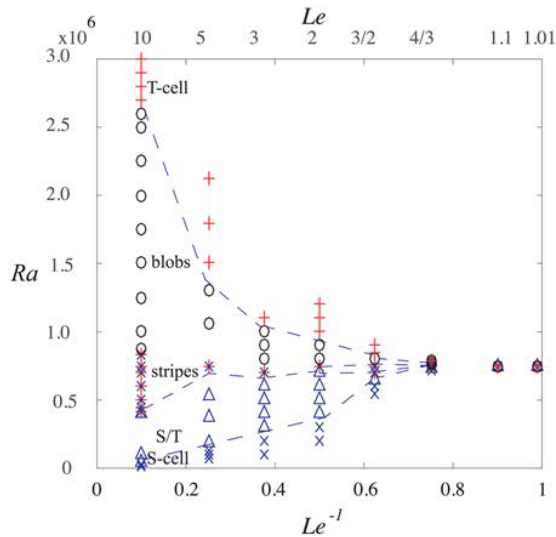


Figure 3 Ranges of the patterns versus Le^{-1} for $Ras = 7.5 \times 10^5$, $Pr = 1$ and $L/D = 8$. Corresponding values of Le are given at the top. Symbols as in figure 2. (Colour online)

Some runs take very much longer than others to run. At the single point values, the extremely long growth times from one pattern to another required times of 100 or more. In addition, the flows at parameters close to the transition values take the longest time to calculate. Not only are growth rates very small, but some flows near transition are characterised by oscillations (not always completely periodic) with a very long period. Therefore, the line locations indicating transitions in figures 2 and 3 are not precisely determined and known only to a few percent. It is important to note that the possibility of abrupt transitions with hysteresis at each transition cannot be excluded in these results. Special codes would be needed for proper resolution close to each transition.

3.2.1. The T cell

The next five subsections describe details of each of the flow patterns. The first flow for large Ra/Ras (figure 4) has a flow field that is virtually the same as flows driven by T alone. We name this a T -cell. Fluid at the bottom of the cold end sinks and then spreads toward the other end as a deep current. It uniformly rises up through mid-depth. The rising fluid feeds into T and S boundary layers with different thickness. Up to $Ra = 10^6$, this flow is similar to known flows in smaller aspect ratio chambers. (Rossby 1965, Beardsley and Festa, Rossby 1998, Hughes and Griffiths 2008) but above approximately 10^6 two circulation cells develop (figure 5). A hint of the second cell is visible even with aspect ratio 1 in Rossby's (1998) figure 1 at $Ra = 10^7$ and 10^8 . After some analysis, we conclude that the dynamic reason for the second cell is that strong downward flow along the left wall pulls warmer fluid down and this generates positive vorticity next to the sinking region (figure 5(e),(f)). This produces vorticity opposite in sign from the vorticity of the sinking plume that drives a counter cell at mid-depth.

Although the ocean itself is not discussed in this section, location of a guess for the ocean parameters are shown in figure 2. In the spirit of Munk (1966), these are based on a

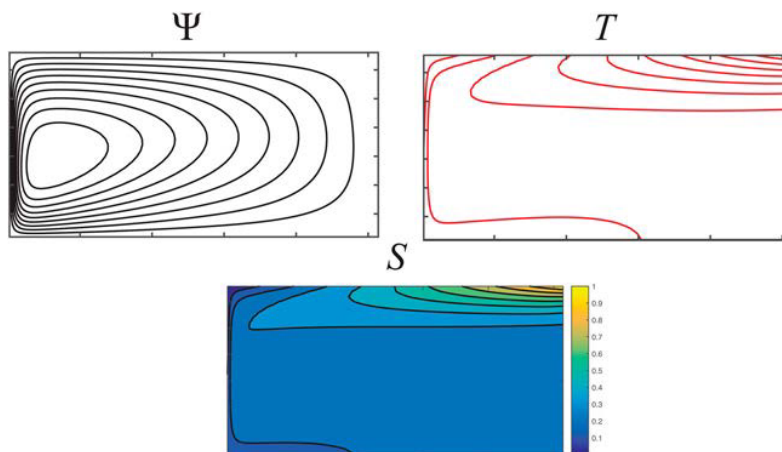


Figure 4 A steady T -cell with a sizeable correction from salinity. Vertical axis is stretched by 4 to help visualisation. (a) Contours of streamfunction (normalised by the maximum), (b) Nine equally spaced contours of T and (c) Nine equally spaced contours of S . $Ra = 4 \times 10^5$, $Ras = 2 \times 10^5$, $Le = 2$, $Pr = 1$ and $L/D = 8$. (Colour online)

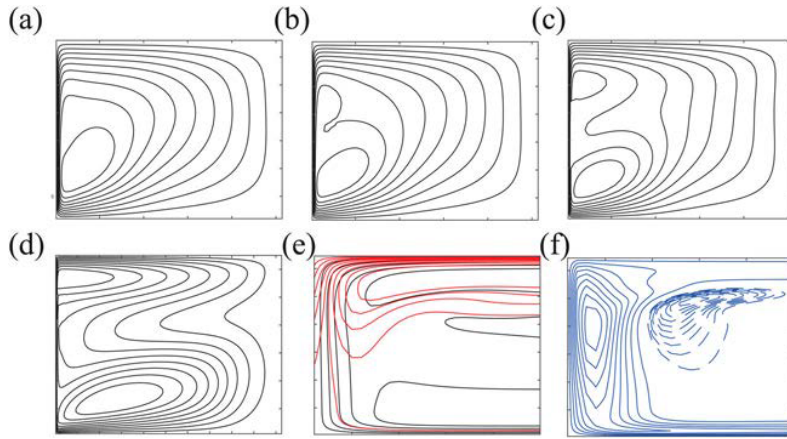


Figure 5 Ten contours of streamfunction (equally spaced and normalised by the maximum value) at larger values of Ra . The flow is driven almost completely by T . $Ras = 10^{-3}$, $Pr = 1$ $L/D = 8$. (a-d) The vertical axis stretched by 4 to allow clearer viewing of the deep flow. (a) $Ra = 10^6$, (b) $Ra = 2 \times 10^6$, (c) $Ra = 5 \times 10^6$, (d) $Ra = 10^8$ (e and f) Close-up of the flow in (d) in a region of width 1 at the left end (vertical axis not stretched). This is from high resolution 128 by 1,024 grid calculations. (e) The streamfunction is black with 25 equally spaced values and temperature is red with isotherms 0.04 apart. (f) contours of vorticity. Negative values are solid and positive values are dashed. (Colour online)

thermal boundary layer thickness of about $1/4$. Here, the salinity contributes about 33% of the density variation and a value of Le of about 2 is used. All these factors and their suitable application to the ocean are discussed more fully in section 5.1.

3.2.2. Blobs

The blobs in the designated regions of figures 2 and 3 have a large scale flow identical to the T-cell with the addition that one or more time-dependent blobs repeatedly form under the surface at the hot salty end and are swept as they grow by the large-scale flow to the cold fresh end. The blobs have locally high salinity and this feature causes cyclic flow by speeding up the circulation when a blob reaches the cold sinking plume. An element of randomness for the formation of each new blob makes flows that are not strictly periodic in time.

A blob is a small body of saltier warmer water originating at the top of the salty end (figure 6). The form appears superficially to resemble a solitary wave because blobs are often spaced far apart, but no suitable mathematical expression has been found. Each individual blob is advected along the top from the hot salty end to the cold fresh end. It increases in size and sinks down as it moves along (figure 7(a),(b)). It has a local inversion in density (figure 6(a),(e)) at its base. The arrival of a salty blob at the sinking cold region triggers the spikes in the maximum value of streamfunction in the chamber in figures 6 and 7 (also see Movie 1.mov).

A blob grows in a manner similar to both the sinking within the classical salt fountain (Stommel *et al.* 1953) and to a sinking region of a salt finger (Schmitt 1994). figure 8 (unstretched coordinates) has arrows showing the diffusive buoyancy flux calculated at each grid point in a blob. It shows that the buoyancy flux of warm temperature (upward

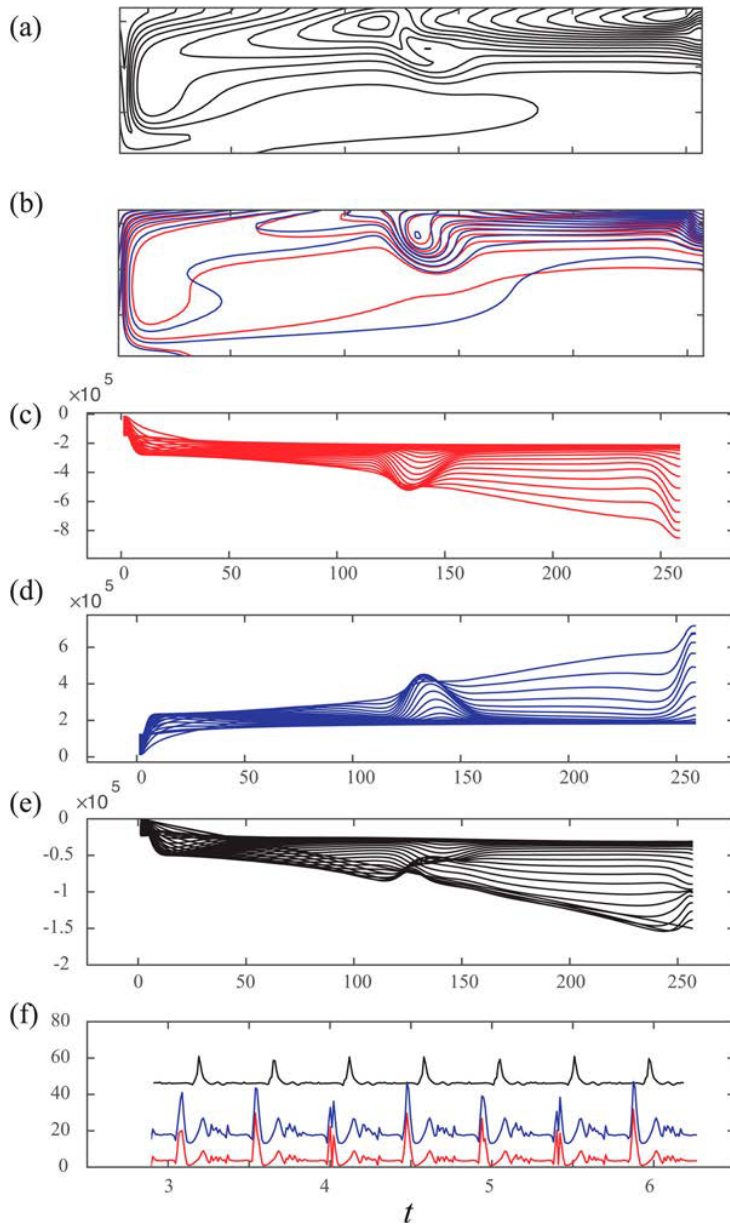


Figure 6 Flow containing a blob that is travelling from right to left in the top current. Vertical distance is stretched by 2 in (a) and (b). (a) Contours of density ($RaS - RaT$). (b) Contours of T (red) and S (blue). (c) Density due to temperature alone across the chamber at ten depths that are equally spaced top to bottom. (d) Density due to salinity alone across the chamber at the same ten depths. (e) Total density across the chamber at the same ten depths. (f) Values over time of S (with 0.3 subtracted and then multiplied by 100) at the middle of the top (blue), and T (offset by 0.5 and amplified by 100) at the middle of the top (red). Also, the maximum absolute values of the streamfunction in the chamber (black). $Ra = 9 \times 10^5$, $RaS = 7.5 \times 10^5$, $Le = 2$, $Pr = 1$ and $L/D = 8$. (Colour online)

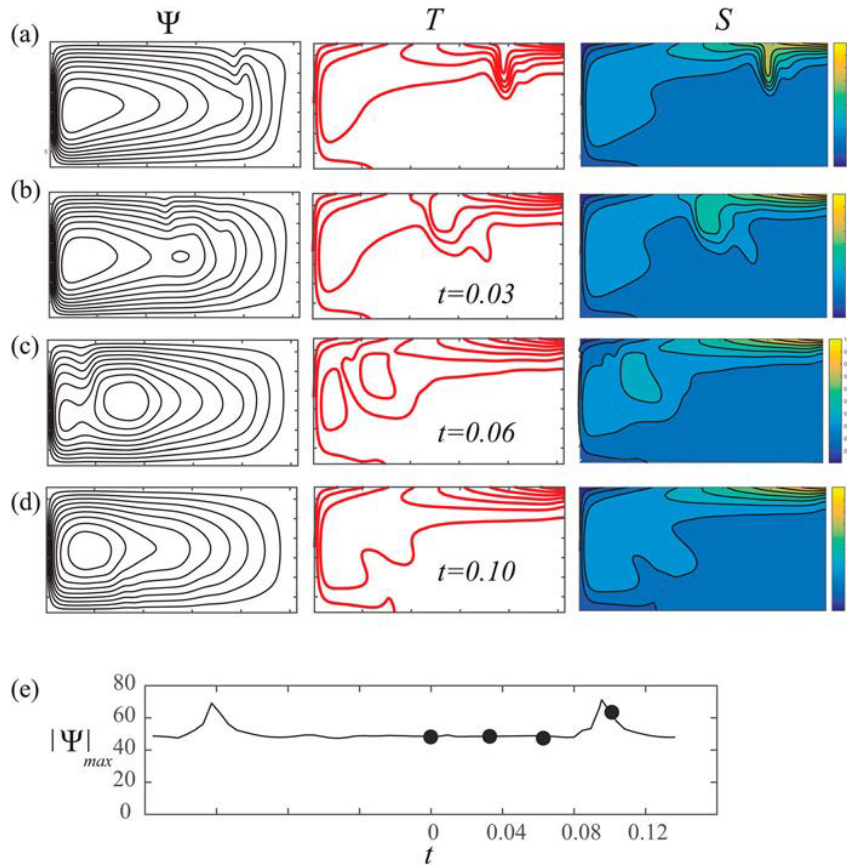


Figure 7 Results for a blob at four times that travels along the top from the hot salty end to the cold fresh end. Panels show streamfunction, (left column, normalised by the maximum value), T (middle column, there are 9 red isotherms) and S (right column, there are 9 black isopleths). The times of (a-d) are indicated by the solid circles in (e), which shows the maximum absolute value of the streamfunction in the chamber over time. Panels in (a-d) are stretched by 4 in the vertical direction to allow clearer visualisation. $Ra = 8.3 \times 10^5$, $Ras = 7.5 \times 10^5$, $Le = 2$, $Pr = 1$ and $L/D = 8$. (Colour online)

buoyancy) away from the blob is greater than the buoyancy flux of excess salinity, (downward buoyancy). Therefore, the buoyancy flux increases the density contrast between the blob and ambient fluid over time and perpetuates the sinking. The blobs are not narrow like salt fingers (generally salt fingers are considered for larger values of Le), but these appear to be as wide as the top thermal boundary layer. Attempts to link blobs to length scales of salt fingers are presently unsuccessful, probably because stratification is not uniform. In spite of numerous runs, the value of Ra/Ras for transition from the T-cell to blobs is poorly resolved. The estimate is difficult because when Ra/Ras of a T-cell is slowly decreased, blobs first emerge as individual events separated by an extremely a long time interval, in some cases ten times longer than the interval in figure 7. The transition to a blob can be helped by introducing a disturbance to trigger the first blob. This implies that the transition involves

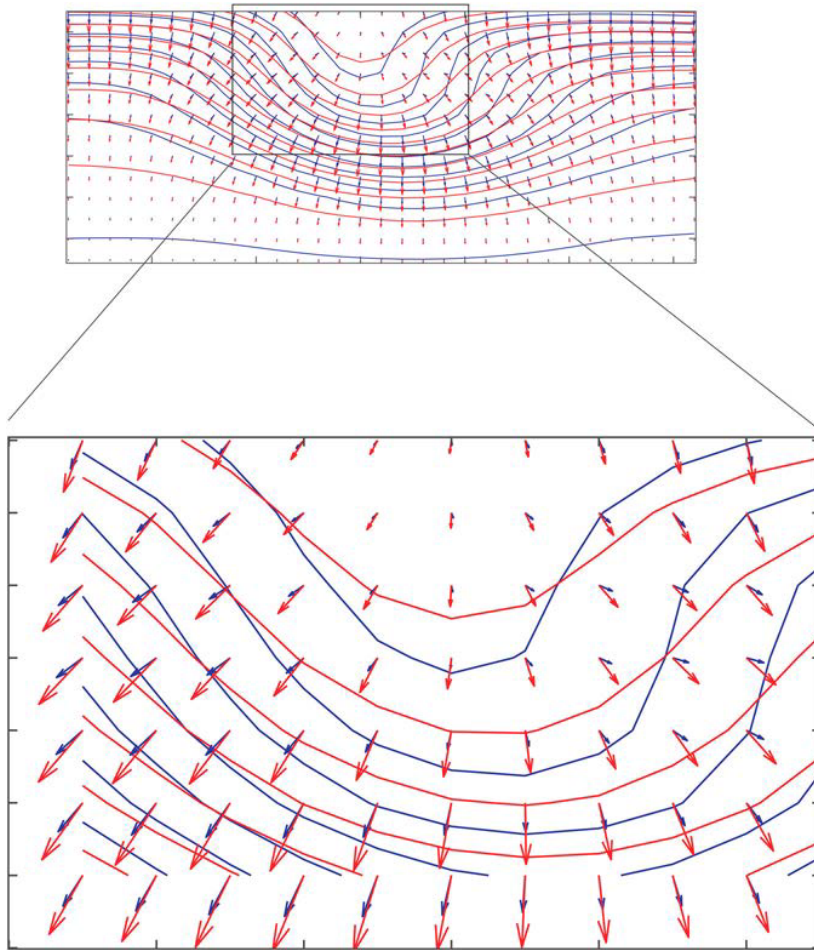


Figure 8 Vectors of diffusive buoyancy flux within a blob at the top due to salinity ($Le^{-1}Ra_S\nabla S$ blue arrows) and for heat ($Ra\nabla T$ red arrows). The bottom panel is a close-up showing that buoyancy flux of heat away in red exceeds that of salinity in blue. Therefore, the rate of increase in density of the blob from cooling exceeds the rate of decrease in density due to freshening. The rate of overall density change is positive and density of the blob increases in time. $Ra = 9 \times 10^5$, $Ra_S = 7.5 \times 10^5$, $Le = 2$, $Pr = 1$ and $L/D = 8$. (Colour online)

a finite amplitude instability. For further decrease from the T cell into the blob regime, the time interval between blobs shrinks and finally many blobs follow each other closely.

3.2.3. The stripes pattern

The third pattern (stripes) occurs where the buoyancy forces of T and S are almost the same size. The regions in parameter space in figures 2 and 3 for stripes are located close to $Ra/Ra_S \cong 1$ at $Ra \geq 10^4$ and $Le \geq 2$, with an extremely narrow range with $Le = 2$ but much wider ranges up to $Le = 10$. One way to observe the formation of stripes is to slowly decrease Ra/Ra_S starting with a flow with blobs. Gradually, each blob develops more buoyancy until one finally reaches to the bottom. At that instant, the movement of the blob

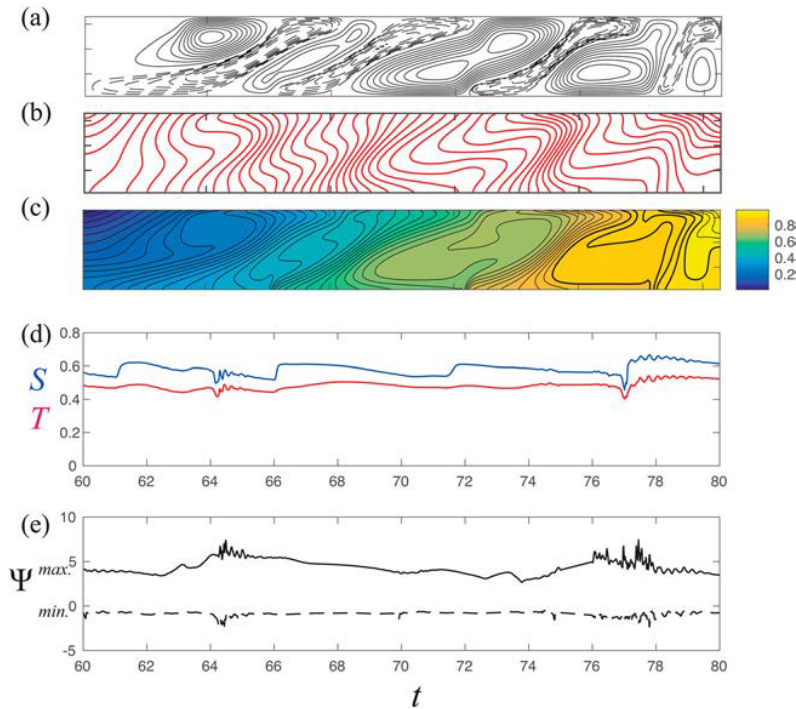


Figure 9 The stripes pattern (a) Vertical section with streamfunction contours (clockwise circulation has black dashed, and counterclockwise circulation has black solid). (b) Isotherms (every 0.02). (c) Salinity contours (every 0.02). (d) Values over time of S at the middle of the bottom (blue) and of T at the middle of the bottom (red). (e) Maximum (solid) and minimum (dashed) values of the streamfunction changing with time. $Ra = Ras = 2 \times 10^5$, $Le = 10$, $Pr = 1$, $L/D = 8$. (Colour online)

along the top stops. Slowly thereafter, the quasi-steady pattern shown in figure 9 forms with each cell extending from top to bottom. The cells have alternating sign of circulation along the chamber with all of them tilted with their top leaning toward the hot salty end. For each pair, one cell has the clockwise circulation of the S -cell and it is clearly narrower than the other, which has circulation of the T -cell. The different widths can be attributed to the smaller diffusivity in the ranges shown in figures 2 and 3 (although some are exceptions to the general rule are found at smaller Ra). Each cell has a center that is stirred by repeated overturning and mixed by diffusion so they end up with relatively constant values of S . The values of T and S become higher in a stepwise manner from the cold fresh end to the hot salty end. The cells rearrange slowly with some growing and others decaying thus generating the time series shown in figure 9, and in most cases cells of both signs move to the left. (see Movie 2.mov). This produces cycles that have periods of many time units. Therefore, the cycle time is typically longer than the blob cycle times.

The dynamics of the stripes is simple to understand. This pattern exists in a parameter range where buoyancy from the fields of T and S almost cancel each other. This produces very slow flow; (note the small values of ψ in figure 9(e) compared to figure 7(e)). Although

a full theory has not been developed, it can be suggested that the cells transport both T and S down the lateral gradient more effectively than diffusion.

3.2.4. The S/T pattern

The fourth pattern, at even smaller Ra ($< Ras$) is called the S/T pattern (figure 10). This occurs if the flow starts in the stripes pattern and then Ra/Ras is slowly decreased until the tops of the T -cells in the stripes cell don't quite reach to the top. In this case, a large overturning and shallow S -cell forms along the entire top region of the cell. Below this cell, small counterclockwise T -cells form along the bottom. Because of the smaller diffusivity of S , the change of buoyancy from S along the bottom is smaller than the change of buoyancy of T and this, along with a destabilising temperature near the bottom provides torque for T driving the circulation of each cell. The bottom cells are advected along the bottom toward the cold end by the bottom current that has the same direction as the bottom of the S -cell. Each cell weakens and ultimately vanishes as it approaches the cold end and another cell forms and grows at the warm end, thus generating a periodic time dependence of T and S (figure 10(d),(e), see Movie 3.mov). The bottom cells in this figure extend up to half way above the bottom, but in other cases the cells do not extend as high. Close to the marginal

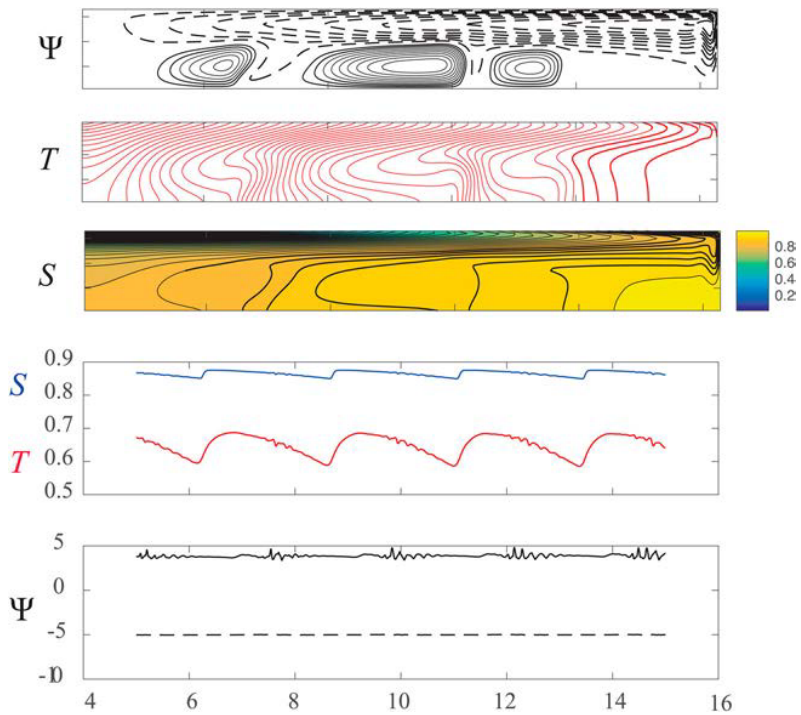


Figure 10 The S/T pattern. (a) Vertical section with streamfunction contours (clockwise circulation is black dashed, and counterclockwise circulation is black solid). (b) Isotherms. (c) Salinity contours. (d) Values over time of S at the middle of the bottom (blue), of T at the middle of the bottom (red). (e) Maximum (solid) and minimum (dashed) values of the streamfunction. $Ra = 1.5 \times 10^5$, $Ras = 7.5 \times 10^5$, $Le = 10$, $Pe = 1$, $L/D = 8$. (Colour online)

region (near the S-cell in figure 2), only a single bottom cell appears and disappears. As with the other patterns this irregular behaviour makes the determination of exact marginal values difficult to precisely determine.

3.2.5. The S cell

The S-cell (figure 11), is found if Ra is substantially less than Ras . Because local Reynolds number is 48 or less, descending flow is steady and consists of a concentrated sinking salty laminar flow that feeds a bottom return pathway. A boundary layer occupies the top of the rest of the chamber with the well-known balance between advection from a slow broad upwelling flow and downward diffusion of “freshness” (lower salinity).

3.3. Resolution

In addition to the work described in the Appendix, resolution was tested using comparison of two time dependent records for $\max|\psi|$ using two different grid sizes (figure 12) from identical beginnings. Comparison of the time series gives a measure of the sensitivity of the variables to grid size. This parameter group ($Ra = Ras = 7.5 \times 10^5$, $Le = 10$, $L/D = 8$) is particularly good for a comparison because flows initially become complicated and very time dependent with lots of eddies. One record has a 32×256 grid and the other is finer (64×512), (it also requires a correspondingly smaller time step). Up to almost $t = 0.1$, the shape of the time dependent curves is identical although the amplitude of the finer scale is a few percent larger in magnitude. Then, the two records become less coherent although the features are similar. Both records develop flow with a primary and secondary frequency until about $t = 0.3$, and after that, there are about 30 spikes roughly every 0.01 time units apart of assorted amplitudes. This shows that resolution for the two grid sizes is good enough to produce almost perfect agreement except for a difference in amplitude until $t = 0.1$. Then, the results are quantitatively different in detail. They still appear to have the same statistical features. In this run, the flow settles down to the stripes pattern after $t = 10$ with virtually identical patterns. The appendix has further details about resolution.

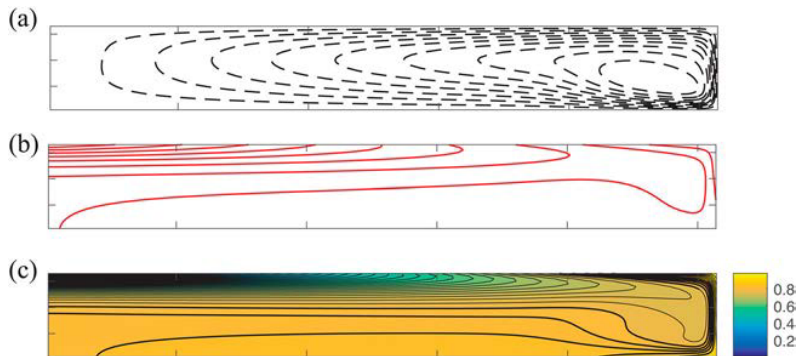


Figure 11 Vertical sections of the S-cell. (a) Contours of ψ . (b) Contours of T . (c) Contours of S . $Ra = 0.001$, $Ras = 3.75 \times 10^5$, $Le = 0.5$, $Pr = 1$, $L/D = 8$. (Colour online)

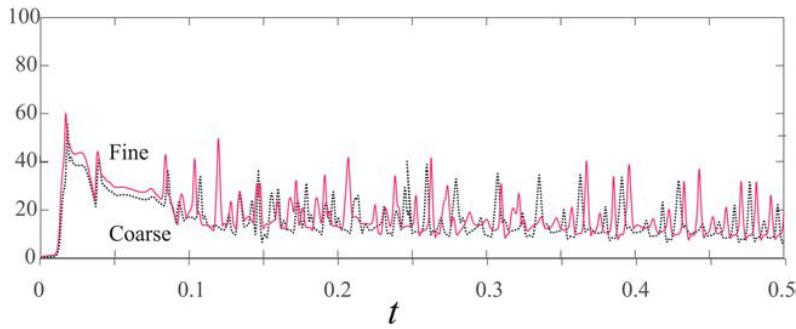


Figure 12 Time series of the maximum absolute value of streamfunction for coarse (dotted black) and fine (solid red) grids. $Ra = Ras = 7.5 \times 10^5$, $Le = 10$, $L/D = 8$. (Colour online)

4 Balanced flow

Balanced flow ($Ra = Ras$) shows the effects of differential diffusion vividly because the imposed densities exactly compensate each other at the boundary and the only alteration to density occurs from differential diffusion in the interior. This section shows calculations from a wide range of values of Ra and Ras .

First, there is “small” Ra and Ras (< 8900) with $L/D = 8$ and $Le > 1$. All results seem the same as here. With a calculation starting from initial conditions $T = S = 0.5$, the circulation initially develops as at T-cell since T diffuses down into the fluid more rapidly than S . However, as time progresses, both fields become the same and flow amplitude shrinks to zero. This is stable because a numerical perturbation introduced to this balance relaxes to a train of cells moving from the hot salty end to the cold fresh end and amplitude decays exponentially in time. The decaying cells are not shown because they have the same form as flow above $Ra = Ras = 8900 \pm 50$, where the decay rate changes sign and the perturbation grows (figure 13). For this instability, the perturbation was presumably from truncation error noise that is of order 10^{-16} . Growth is slow and finite size emerges in about 50 time units. (The fun of numerical work is that this growing pattern is readily seen by subtracting the mean). This pattern also occurs for larger values of Ra and Ras with T - and S -cells lying side-by-side. Aspect ratios range 0.5–3 up to $Ra = Ras = 10^5$. Close to critical they move from right to left, but approaching the larger values of Ra and Ras the cells move around irregularly.

As shown in section 3.3.3, the cells become stripes in the range $10^5 \leq Ra = Ras \leq 10^6$. Above this range, the stripes change to a new pattern called a supercell, which will be described next. The transition value of stripes to supercell has been proven to be difficult to document precisely with the balanced flow at $Le = 2$, but at larger Le the transition is distinct. Supercells are always seen at $10^6 \leq Ra = Ras \leq 10^8$ (figure 14).

Supercells are inherently time-dependent with numerous small eddies in two principal locations. One location is below the top at the extreme right with numerous eddies similar to blobs. The second is the middle level with eddies within the S cell that extends from lower left to upper right. The S-cell deforms, vanishes occasionally and then returns, leading to the great time fluctuations in large-scale properties shown in figure 14(d)–(f).

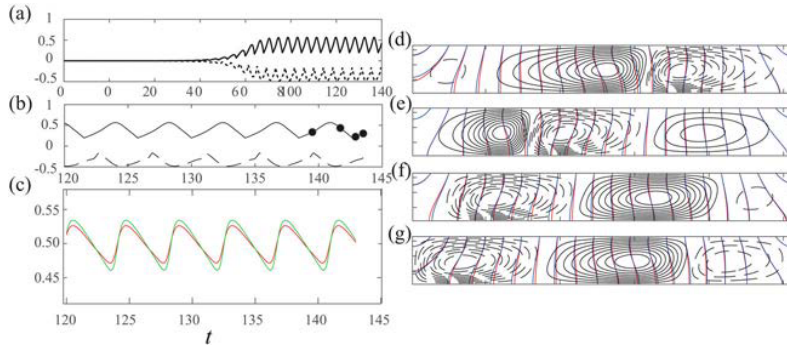


Figure 13 Convection cells at $Ra = Ras = 10^4$, $Le = 2$ and $L/D = 8$. (a) Maximum and minimum values of streamfunction over time as the instability develops. (b) Close-up of steady oscillations in a narrower range than (a). (c) T (red) and S (green) at the middle of the bottom with time. (d-g) Cells at the times shown by dots in (b) Solid black curves are positive streamfunction with ten contours normalised by the maximum value. Dashed black curves are negative streamfunction with the contours normalised by the minimum value. Also shown are 20 isotherms (red) and isohalines (blue). (Colour online)

Nusselt numbers and streamfunction extrema over the entire range for single component and balanced flows are shown in figure 15. Steady flows have values averaged over 0.1 time step accurate to one part in 10^4 from averaging. For unsteady flows, many time steps are generally required for the records to settle to a cyclic pattern. To give a comparison of the values for single component horizontal convection, the flows with negligible salinity (actually, $Ras = 10^{-3}$) and $L/D = 8$ are calculated. The Nusselt Number at $Ra > 10^4$ approaches the line $3.54 \times Ra^{1/5}$ (shown) and the streamfunction maximum approaches a similar slope (shown) at $Ra \geq 10^5$. These are similar to the results for $L/D = 1$ (Rossby 1998), although naturally the coefficients for Nu for ψ_{max} are larger. Balanced flows produce more scattered records. They are always time dependent and the slopes we have obtained so far are gathered by finding maximum and minimum values from time series like those in figure 14. One sees a hint of the 1/5 power law (a line is drawn in) but the values have considerable scatter. Values fall off at $Ra = Rac = 5 \times 10^8$ and are presumed to be near the edge of our practical limit. Time limitations did not permit long time averaging reduce away the scatter, so the results are suggestive rather than definitive.

5 Comparison with other models and possible oceans

5.1. The T cell and scaling considerations

The T-cell is familiar to oceanographers since it resembles an ocean dominated by sinking of a concentrated current of cold fresh water at the cold fresh end. The downwelling feeds a bottom current conveying cold fresh water away from the cold end that feeds into a broad upwelling flow. The colder fresh fluid is warmed by downward conduction of heat so that there is a thermal boundary layer and there is a corresponding salinity boundary layer in this case. Examples of a cold fresh bottom current terminated by an upwelling region are particularly good in the deep ocean, for instance the movement of cold fresh Antarctic

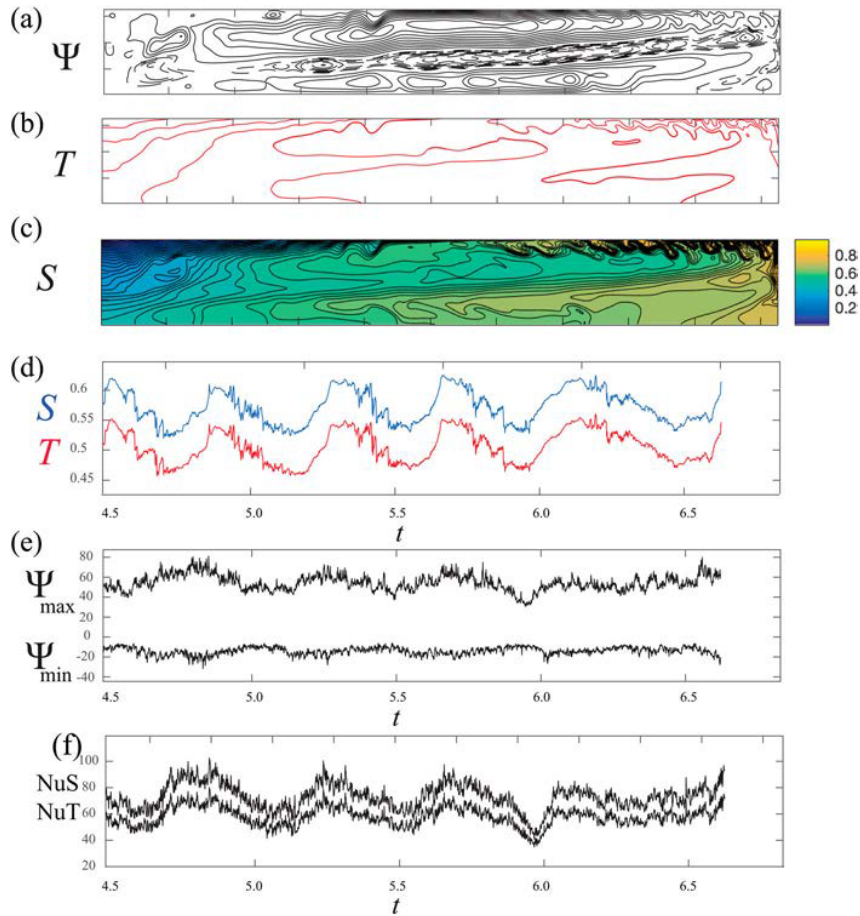


Figure 14 The supercell. (a) Vertical section with streamfunction contours (clockwise circulation has black dashed, and counterclockwise circulation has black solid). (b) Isotherms (every 0.1). (c) Salinity contours (every 0.02). (d) Values over time of S at the middle bottom (blue) and of T at the middle bottom (red). (e) Values over time of the streamfunction maximum (upper curve) and minimum. (f) Nusselt number and Salinity Nusselt numbers over a time span. $Ra = Ras = 10^6$, $Le = 2$, $Pr = 1$, $L/D = 8$. (Colour online)

bottom water into the western Atlantic is like this. In that case, the different mixing rates of T and S have even been estimated (Whitehead and Worthington 1982).

A best fit of our T-cell to the present ocean occurs if the average thermocline depth in the model is proportional to a fraction of the depth of the present oceans. We follow the famous “Abyssal Recipes” (Munk 1966) and fit the depth from our results to the ocean. Since S has smaller diffusivity, the halocline is a little shallower than the thermocline in figure 4. This can only be interpreted loosely for a number of well-known reasons.

The fit also includes the fact that the world’s oceans have a fraction of the density variation from salinity compared to temperature (Sverdrup *et al.* 1942). A crude fit for “typical” values for the ocean is given in figure 2(a). The exhaustive review by Gregg *et al.* 2018

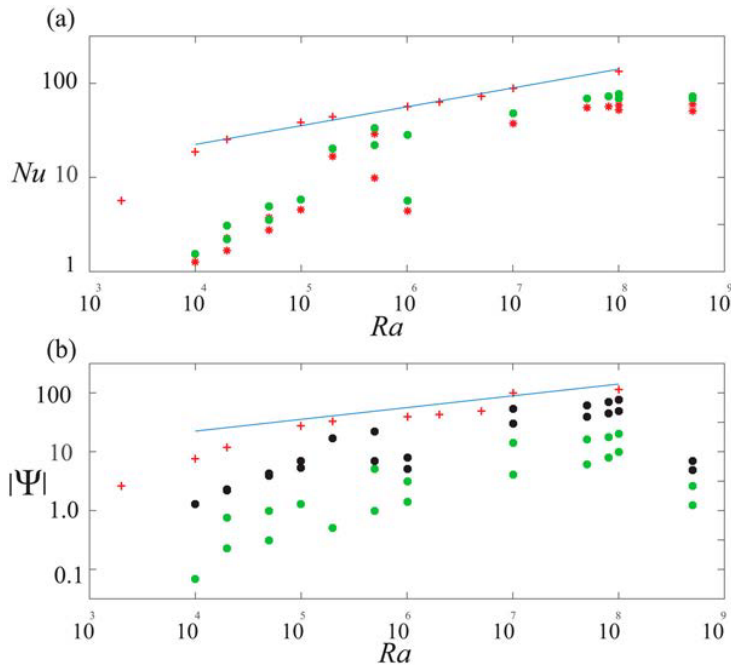


Figure 15 (a) Nusselt number and the equivalent salinity Nusselt number plotted as a function of $Ra (= Ras)$ for $Le = 2$. Two values each indicate the excursions for time-dependent flow. Nu for single component flow (Red+), Nu (red *) and NuS (Green o) for $Ra = Ras$. The line is $3.548Ra^{1/5}$. (b) $\max \psi$ for single component flow (red +), $\max \psi$ (black o), $|\min \psi|$ (green o). A line with $Ra^{1/5}$ slope is drawn in. (Colour online)

examines evidence from laboratory results and direct ocean measurements indicating that the value of Le might be between 1 and 2.

This application to the ocean is interpreted loosely for a number of well-known reasons. First, thermocline depth is not easy to precisely define because depths vary between each basin and even regionally, having values as small as a few hundred metres near the tropics to about 1500 metres in the broad mid-latitude regions. Second, the practical value of ocean depth is somewhat ambiguous and it is different for each basin. Third, of course this model leaves out many important aspects of ocean circulation. Rotational effects introduce completely different scaling laws for the velocity (Park and Whitehead 1999) and wind effects modify thermocline depths by 1–2 km (Gnanadesikan 1999).

5.2. Volume of the masses for the different patterns

The percentage of area with values of T and S between 0 and 1 varies for each of the patterns here with Ra , Ras , and Le being ingredients in determining them. This is relevant to the issue of ocean water masses that are a fundamental property in physical oceanography. For example, at $Le = 1$ there is either a T cell with a large volume of cold fresh deep water or an S cell with a large volume of warm salty deep water depending on values of Ra and Ras . In contrast, for $Le = 2$, there are 5 patterns with different volumetric signatures as in figure 16.

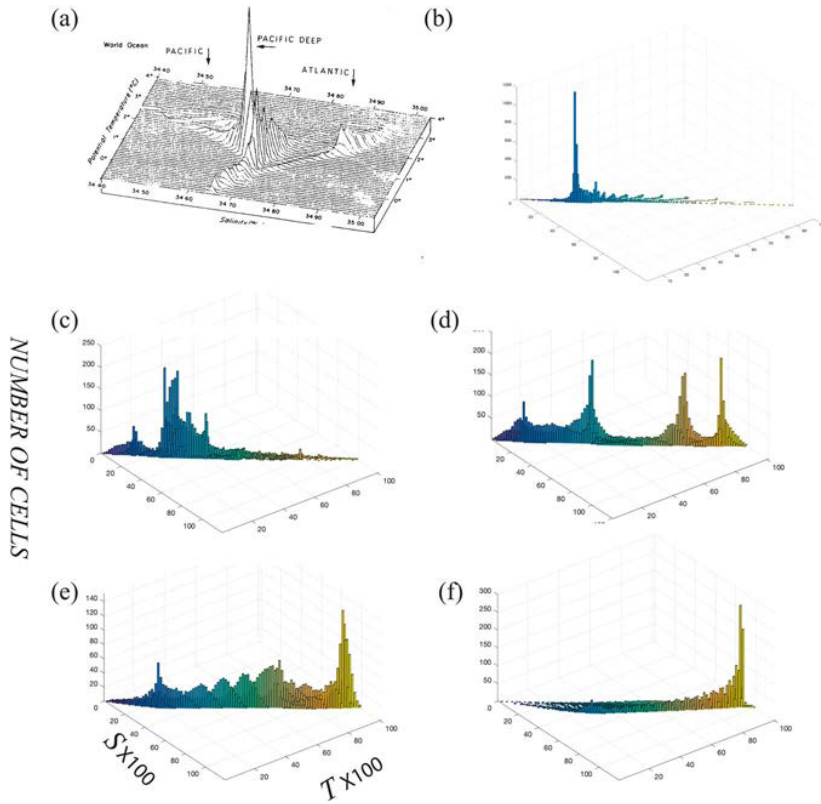


Figure 16 Relative volumes of water mass classes. (a) Volumes for all the oceans of the world (Worthington 1981), and (b-f) from the numerical experiments for the five different flow ranges with $Ras = 3 \times 10^5$, $Le = 2$, and $Ra = 4.5, 3.2, 3.0, 2.8$, and 2.0×10^5 , respectively. (Colour online)

This was produced by plotting the number of grid points from a calculation within each 0.01 interval of T and S . Since even the coarsest grid has $2^{13} = 8192$ points, there are plenty of points in almost all the intervals that are occupied.

I was surprised that differential diffusion flows are largely concentrated along the mixing line because I expected the curve to have much more scatter like the present ocean (figure 16(a) from Worthington 1981). All one can say is that the T-cell distribution in our calculations resembles the distribution in the Atlantic with its large volume of North Atlantic Deep Water that enters from the north. All other features in figure 16(a) (Antarctic Bottom water from the south, scatter from localised polar regions and multiple basin effects) apparently require more complex basin geometry.

5.3. Aspects of a fit to the ocean thermocline

The location of the best fit range of “typical” parameters for $Le = 2$ for the ocean is shown in figure 2(b). This is well within the stability range of the classic T-cell flow and not close in parameter space to a transition to blobs. The flow in this range of Ra is laminar because

Reynolds number Re extends only up to approximately 100. This value is calculated for a run with $Pr=1$, so Re is equal to Peclet number and we use the largest extremum of the streamfunction in (figure 15). Generally, at this Reynolds number, the flow is steady and our calculations are smaller than the values of Re needed to produce turbulence in the sinking plume (Hughes and Griffiths 2006, Hughes *et al.* 2007, Marchal 2007, Hughes and Griffiths 2008, Gayen *et al.* 2013, Hughes *et al.* 2013).

5.4. Summarising remarks

Differential diffusion in horizontal convection has 7 patterns of the full range of these calculations. At low Ra travelling cells occur. Then in the range $10^4 > Ra > 10^6$ there are 5 patterns: T-cell, blobs, stripes, S/T, and the S-cell. Finally, there is the supercell at the largest values of Ra . Only the T and S cells are steady, all the rest are time dependent with the time dependence being of the order of the net thermal time scale D^2/κ or longer. The results are sensitive to Le and insensitive to Pr .

The cycles differ from cycles in previous calculations that use the same numerical code but with mixed Dirichlet-Neumann boundary T - S forcing (Whitehead 2017) and no differential diffusion. In particular, these mixed boundary conditions make abrupt transitions and do not produce the time-dependent patterns found here. A thermal time scale in the ocean of 400 years (a value that is very poorly constrained and might be many times longer) indicates that for the most part cycles like those here, if they exist in the ocean, would occur over at least many hundreds of years. Except for the blobs, those periods are too long to duplicate decadal T/S variations and all of them are too short to duplicate millennial oscillations.

In terms of ocean models, perhaps the cycling flows in a 3×2 box (a matrix of chambers connected by tubes) analysed by Colin De Verdière *et al.* (2006) and Colin De Verdière (2007) have some resemblance to the T-cell cycling with a stripes pattern. Other ocean models (Winton and Sarachek 1993, Paul and Schulz 2002, Arzel *et al.* 2006, Marchal *et al.* 2007) have vigorous T-cell oscillations with speeding up and slowing down. These seem to be driven with variations in properties concentrated at the cold fresh end, but do not possess blobs or eddies with distinct thermohaline signatures. Their periods are faster and the cycles are clearly more complex than the convection studied here and may arise from processes not in our model (e.g. rotational flows, wind stress effects, geometric complexity of the actual ocean basins, and ice dynamics). Unfortunately, such models generally possess different boundary conditions for T and S at the boundaries rather than differential diffusion, so a comparison of our oscillations with those in many numerical models does not have much meaning.

Oscillating convection is common in numerous binary fluid situations found in engineering (e.g. Knobloch 1986) and particularly in linear instability theory. Convection in alcohol-water solutions oscillates and the fluids have diffusivity ratios close to the values used here. However, it is difficult to isolate the source of those oscillations because the experiments also include other processes such as Soret effects, Dufour effects, and equation of state nonlinearities. Much of the theory for oscillation in binary fluids concerns marginal states that might not grow to large oscillations since this happens in in Stommel's 1961 box model and in double diffusion (Veronis 1968).

A laboratory example that might involve differential diffusion has an oscillation cycle that starts with a fully mixed freshwater layer cooled from above (Whitehead *et al.* 2005). The bottom of this layer is an interface with warmer deeper salty water. The surface cooling of the upper layer produces active convection that continues to mix the layer. Gradually, salinity of the upper layer increases from the interface mixing, but the layer temperature stays more constant as the surface cooling is matched by heat flow through the interface. This mixing would follow differential diffusion with the buoyancy flux due to heat flow and salinity flow being unequal. The layer is laterally connected to another layer of warm freshwater over the same warm deep salty water in an adjacent basin and a simple hydrostatic balance for both layers requires that the layer gradually deepens as density increases from salinity increase. Finally, the salinity difference between the cold fresher layer and the deeper warm salty water approaches zero and the layer mixes away. Then warm fresh water flows into the top from the neighbouring layer and a new layer forms, only to be followed by a repeat of the cycle. Clearly, this laboratory flow differs significantly from the horizontal convection with differential diffusion analysed here. Our results have no vertical excursion of a mixed layer and have many lateral eddies. The closest counterpart would be the stripes pattern with alternate T and S cells arriving at the cold end. Calculations in progress with $L/D = 1$ and differential diffusion (Z. Carlo Frontera and O. Marchal, private communication) produce oscillations with T and S cells vertically stacked that might be closer to the laboratory results, and more work is planned.

In summary, these calculations show that differential diffusion in horizontal convection produces time-dependent flows. The T and S fields rearrange themselves into a variety of patterns over wide ranges of the governing parameters. Since such oscillations might occur in the Holocene (Paul and Schulz 2002) the results can be added to the list of increasingly strong arguments for the need to understand the contributions to variability from T and S in the ocean.

Acknowledgements

Funds are provided from an Emeritus expense account by Woods Hole Oceanographic Institution. I particularly want to thank Olivier Marchal for many helpful suggestions.

Disclosure statement

No potential conflict of interest was reported by the author(s).

References

- Arzel, O., Huck, T. and Colin de Verdière, A., The different nature of the interdecadal variability of the thermohaline circulation under mixed and flux boundary conditions. *J. Phys. Oceanogr.* 2006, 36(9), 1703–1718, doi:10.1175/JPO2938.1.
- Beardsley, R.C. and Festa, J.F., A numerical model of convection driven by a surface stress and non-uniform horizontal heating. *J. Phys. Oceanogr.* 1972, 2, 444–455, doi:10.1175/1520-0485(1972)002 < 0444:ANMOCD > 2.0.CO;2.
- Colin De Verdière, A., A simple model of millennial oscillations of the thermohaline circulation. *J. Phys. Oceanogr.* 2007, 37, 1142–1155, doi:10.1175/JPO3056.1.

- Colin De Verdière, A., Jelloul, M.B. and Sévellec, F., Bifurcation structure of thermohaline millennial oscillations. *J. Clim.* 2006, 19, 5777–5795, doi:10.1175/JCLI3950.1.
- Gargett, A.E., Ocean turbulence. *Annu. Rev. Fluid Mech.* 1989, 21, 419–451, doi:10.1146/annurev.fl.21.010189.002223.
- Gargett, A.E., Differential diffusion: an oceanographic primer. *Prog. Oceanogr.* 2003, 56, 559–570, doi:10.1016/S0079-6611(03)00025-9.
- Gargett, A.E., The effects of $KT \neq KS$ in a Stommel-like model of the upper Atlantic Meridional overturning circulation under steady surface flux forcing. *J. Mar. Res.* 2019, 77, 243–266, doi:10.1357/002224019826887353.
- Gargett, A.E. and Ferron, B., The effects of differential vertical diffusion of T and S in a box model of thermohaline circulation. *J. Mar. Res.* 1996, 54(5), 827–866, doi:10.1357/0022240963213628.
- Gargett, A.E. and Holloway, G., Sensitivity of the GFDL model to different diffusivities for heat and salt. *J. Phys. Oceanogr.* 1992, 22(10), 1158–1177, doi:10.1175/1520-0485(1992)022 < 1158:SOTGOM > 2.0.CO;2.
- Gayen, B., Griffiths, R.W., Hughes, G.O. and Saenz, J.A., Energetics of horizontal convection. *J. Fluid Mech.* 2013, 716, R10–1–R10–11, doi:10.1017/jfm.2012.592.
- Gayen, B., Griffiths, R. and Hughes, G., Stability transitions and turbulence in horizontal convection. *J. Fluid Mech.* 2014, 751, 698–724, doi:10.1017/jfm.2014.302.
- Gnanadesikan, A., A simple predictive model for the structure of the oceanic pycnocline. *Science.* 1999, 283(5410), 2077–2079, doi:10.1126/science.283.5410.2077.
- Gregg, M.C., D’Asaro, E.A., Riley, J.J. and Kunze, E., Mixing efficiency in the ocean. *Ann. Rev. Mar. Sci.* 2018, 10(1), 443–473, doi:10.1146/annurev-marine-121916-063643.
- Hirst, A.C. and Cai, W., Sensitivity of a world ocean GCM to changes in subsurface mixing parameterization. *J. Phys. Oceanogr.* 1994, 24, 1256–1279, doi:10.1175/1520-0485(1994)024 < 1256:SOAWOG > 2.0.CO;2.
- Hughes, G.O. and Griffiths, R.W., A simple convective model of the global overturning circulation, including effects of entrainment into sinking regions. *Ocean Model.* 2006, 12, 46–79, doi:10.1016/j.ocemod.2005.04.001.
- Hughes, G.O. and Griffiths, R.W., Horizontal convection. *Annu. Rev. Fluid Mech.* 2008, 40, 185–208, doi:10.1146/annurev.fluid.40.111406.102148.
- Hughes, G.O., Griffiths, R.W., Mullarney, J.C. and Peterson, W.H., A theoretical model for horizontal convection at high Rayleigh number. *J. Fluid Mech.* 2007, 581, 251–276, doi:10.1017/S0022112007005630.
- Hughes, G.O., Gayen, B. and Griffiths, R.W., Available potential energy in Rayleigh-Benard convection. *J. Fluid Mech.* 2013, 729, 1–10, doi:10.1017/jfm.2013.353.
- Knobloch, E., Oscillatory convection in binary mixtures. *Phys. Rev. A.* 1986, 34, 1538–1549, doi:10.1103/PhysRevA.34.1538.
- Marchal, O., Particle transport in horizontal convection: implications for the Sandstrom theorem. *Tellus A: Dyn. Meteorol. Oceanogr.* 2007, 59, 141–154, doi:10.1111/j.1600-0870.2006.00193.x.
- Marchal, O., Jackson, C., Nilsson, J., Paul, A. and Stocker, T.F., Buoyancy-driven flow and nature of vertical mixing in a zonally averaged model. In *Ocean Circulation: Mechanisms and Impacts—Past and Future Changes of Meridional Overturning*, edited by A. Schmittner, J.C. Chiang and S.R. Hemming, pp. 33–52, 2007. (Geophys. Monogr. Ser., vol. 173, 392 pp., AGU: Washington, D.C.). doi:10.1029/173GM05.
- Marshall, J. and Speer, K., Closure of the meridional overturning circulation through Southern Ocean upwelling. *Nat. Geosci.* 2012, 5, 171–180, doi:10.1038/ngeo1391.
- Merryfield, W.J., Holloway, G. and Gargett, A.E., A global ocean model with double-diffusive mixing. *J. Phys. Oceanogr.* 1999, 29, 1124–1142, doi:10.1175/1520-0485(1999)029 < 1124:AGOMWD > 2.0.CO;2.
- Munk, W., Abyssal recipes. *Deep Sea Res.* 1966, 13, 707–730.
- Nishimura, T. and Morega, A. M., Influence of Lewis number on double-diffusive convection in a square cavity filled with binary gas. *Heat Transfer?Asian Res.* 2003, 32, 85–97, doi:10.1002/htj.10073.

- Paparella, F. and Young, W., Horizontal convection is non-turbulent. *J. Fluid Mech.* 2002, 466, 205–214, doi:10.1017/S0022112002001313.
- Park, Y.G. and Whitehead, J.A., Rotating convection driven by differential bottom heating*. *J. Phys. Oceanogr.* 1999, 29, 1208–1220, doi:10.1175/1520-0485(1999)029 < 1208:RCDBDB > 2.0.CO;2.
- Paul, A. and Schulz, M., Holocene climate variability on centennial-to-millennial time scales: 2. internal and forced oscillations as possible causes. In *Climate Development and History of the North Atlantic Realm*, edited by G. Wefer, W. Berger, K.E. Behre and E. Jansen, pp. 55–73, 2002. (Springer-Verlag: Berlin Heidelberg).
- Rehmann, C.R. and Gargett, A.E., *Differential Diffusion*, 2018. (New York: Elsevier Press).
- Rehmann, C.R. and Koseff, J.R., Mean potential energy change in stratified grid turbulence. *Dyn. Atmos. Oceans.* 2004, 37, 271–294, doi:10.1016/j.dynatmoce.2003.09.001.
- Rosby, H.T., On thermal convection driven by nonuniform heating from below: an experimental study. *Deep-Sea Res.* 1965, 12, 9–16.
- Rosby, H.T., Numerical experiments with a fluid heated non-uniformly from below. *Tellus A: Dyn. Meteorol. Oceanogr.* 1998, 50, 242–257, doi:10.3402/tellusa.v50i2.14523.
- Schmitt, R.W., Double diffusion in oceanography. *Annu. Rev. Fluid Mech.* 1994, 26, 255–285, doi:10.1146/annurev.fl.26.010194.001351.
- Scotti, A. and White, B., Is horizontal convection really “non-turbulent?”. *Geophys. Res. Lett.* 2011, 38(21), 1–5, L21609, doi:10.1029/2011GL049701.
- Smyth, W., Nash, J. and Moun, J., Differential diffusion in breaking Kelvin-Helmholtz billows. *J. Phys. Oceanogr.* 2005, 35, 1004–1022.
- Stern, M.E., *Ocean Circulation Physics*, 1975. (New York: Academic Press).
- Stommel, H., Thermohaline convection with two stable regimes of flow. *Tellus.* 1961, 3, 224–230.
- Stommel, H., Arons, A. and Blanchard, D., An oceanographical curiosity: the perpetual salt fountain. *Deep Sea Res.* 1953, 3, 152–153, doi:10.1016/0146-6313(56)90095-8.
- Sverdrup, H.U., Johnson, M.W. and Fleming, R.H., *The Oceans, Their Physics, Chemistry, and General Biology*, 1942. (New York: Prentice-Hall). <http://ark.cdlib.org/ark:/13030/kt167nb66r/>.
- Turner, J.S., The influence of molecular diffusivity on turbulent entrainment across a density interface. *J. Fluid Mech.* 1968, 33, 639–656, doi:10.1017/S002211206800159X.
- Turner, J.S., *Buoyancy Effects in Fluids*, 1973. (Cambridge: Cambridge University Press). UK 368 p.
- Veronis, G., Effect of a stabilizing gradient of solute on thermal convection. *J. Fluid Mech.* 1968, 34(2), 315–336, doi:10.1017/S0022112068001916.
- Welander, P., A new type of double-diffusive instability? *Tellus A: Dyn. Meteorol. Oceanogr.* 1989, 41, 66–72, doi:10.3402/tellusa.v41i1.11821.
- Whitehead, J.A., Abrupt transitions and hysteresis in thermohaline laboratory models. *J. Phys. Oceanogr.* 2009, 39(5), 1231–1243, doi:10.1175/2008JPO4087.1.
- Whitehead, J.A., *Laboratory Studies of Turbulent Mixing*, 2016. (Elsevier: Reference Module in Earth Systems and Environmental Sciences).
- Whitehead, J.A., Convection driven by temperature and composition flux with the same diffusivity. *Geophys. Astrophys. Fluid Dyn.* 2017, 111(4), 229–248, doi:10.1080/03091929.2017.1333608.
- Whitehead, J.A. Jr. and Worthington, L.V., The flux and mixing rates of Antarctic bottom water within the North Atlantic. *J. Geophys. Res.* 1982, 87(C10), 7903–7924, doi:10.1029/JC087iC10p07903.
- Whitehead, J.A., Te Raa, L., Tozuka, T., Keller, J.B. and Bradley, K., Laboratory observations and simple models of slow oscillations in cooled salt-stratified bodies. *Tellus A.* 2005, 57(57A), 798–809, doi:10.1111/j.1600-0870.2005.00150.x.
- Whitehead, J.A., Cotel, A., Hart, S., Lithgow-Bertelloni, C. and Newsome, W., Numerical calculations of two-dimensional large Prandtl number convection in a box. *J. Fluid Mech.* 2013, 729, 584–602, doi:10.1017/jfm.2013.330.
- Winters, K.B. and Young, W.R., Available potential energy and buoyancy variance in horizontal convection. *J. Fluid Mech.* 2009, 629, 221–230, doi:10.1017/S0022112009006685.
- Winton, M. and Sarachek, E. S., Thermohaline oscillations induced by strong steady salinity forcing of ocean general circulation. *J. Phys. Oceanogr.* 1993, 23(7), 1389–1410, < 1389:TOIBSS > 2.0.CO;2.

Worthington, L.V., The water masses of the world ocean: some results of a fine-scale census. In *Evolution of Physical Oceanography*, edited by B.A. Warren and C. Wunsch, pp. 42–69, 1981. (M.I.T. Press: Cambridge, MA).

Appendix The equations and their integration

As in Whitehead *et al.* (2013) and Whitehead (2017), equations for the Boussinesq approximations to the incompressible continuity equation, the Navier-Stokes equations, and conservation of heat and salinity are, respectively

$$\nabla' \cdot \mathbf{u} = 0, \quad (\text{A.1})$$

$$\frac{1}{Pr} \left[\frac{\partial}{\partial t'} + \mathbf{u} \cdot \nabla' \right] \mathbf{u} = -\nabla' p' + \rho_0 g (\hat{T}' - \beta S') \hat{z} \quad (\text{A.2})$$

$$\frac{\partial T'}{\partial t'} + \mathbf{u} \cdot \nabla' T' = \kappa \nabla'^2 T' \quad (\text{A.3})$$

$$\frac{\partial S'}{\partial t'} + \mathbf{u} \cdot \nabla' S' = \kappa_S \nabla'^2 S' \quad (\text{A.4})$$

Prime denotes dimensional quantities for the velocity vector \mathbf{u} ; the time t' , the coordinate in the lateral direction x' , the coordinate with unit vector \hat{z} in the vertical direction z' , the temperature T' , and the salinity S' . The other symbols are the average density ρ_0 , the kinematic viscosity ν , the acceleration of gravity g , the coefficient of thermal expansion β , the coefficient of density increase by salinity β_S ; and finally κ is thermal and κ_S is salinity diffusivity.

Dimensionless equations are derived using the length scale D , the velocity scale κ/D , temperature scale ΔT , salinity scale ΔS and time scale D^2/κ . The three governing parameters are the Rayleigh number $Ra = g \Delta T D^3 / \kappa \nu$, the salinity Rayleigh number $Ras = -g \beta \Delta S D^3 / \kappa \nu$, the Lewis number $Le = \kappa / \kappa_S$ and the Prandtl number $Pr = \nu / \kappa$. Dimensionless equations (1)–(4) are the result.

The chamber is numerically represented as a rectangular grid. Initially ψ , T , and S are a constant value in the grid points except that along the top row T and S linearly change from 0 at the left end to 1 at the right. An external line of grid points is added along the sides and bottom. They physically correspond to a thin layer of solid. In this layer, the value of conductive or diffusive flux is set to zero by setting the grid value equal to the value in the external grid point next to it. This produces zero flux along the sides and bottom with error at the numerical truncation order of 10^{-17} and the total heat or diffused substance is conserved over the entire time of the longest numerical calculation with error of less than 10^{-14} (Whitehead 2017). This method of imposing zero flux at the boundaries is superior by approximately 8 orders of magnitude to using one-sided difference equations to set flux equal to zero.

To advance in time, equations (1) and (2) for temperature, and salinity distributions are stepped forward using a leapfrog-trapezoidal scheme for each time step δt . Lateral flux of heat and salinity are set to zero through the two sides and through the bottom. The equation at each time step depends on whether Pr is finite or infinite. If Pr is finite, the vorticity calculation (3) is stepped ahead in time. For infinite Pr , no time step is needed and instead of (3) a standard Poisson equation solver is used for vorticity. In both cases, (4) for streamfunction is solved using the same Poisson solver. In all cases, free slip (zero vorticity) and zero streamfunction is set on all four sides. The time step is repeated numerous times to find the evolution of the temperature, salinity and velocity fields.

The bulk of the computations use a 32×256 grid, although in cases where precision is needed, and for most of the figures, double the number is used. The same qualitative results are found for all grid sizes, so improved precision does not change the structure of the modes or their approximate

regions in parameter space. This also is found in previous results with a similar programme (Whitehead *et al.* 2013, Whitehead 2017). For example, at $Ra = 10^6$ the vorticity in a square 64×64 grid has the same pattern but a maximum value that is ~ 1.8 higher than vorticity on a 128 grid at the same instant, and that value is ~ 0.6 higher than a 256 grid (Whitehead *et al.* 2013). However, if in future studies internal speeds become large enough for Reynolds number Re to attain a size above 100, shear instability will occur and the fluctuations will be increasingly energetic with finer resolution. The present calculations have at most $Re = 100$ and therefore are not conducted with large enough Re for this to be true.